Materials Advances

PAPER

View Article Online
View Journal | View Issue

Check for updates

Cite this: *Mater. Adv.*, 2025, 6, 388

Interplay of plasmonic and charge transfer effects for ultrasensitive Ag–WO_3/TiO_2 photonic crystal SERS sensors†

Maria-Athina Apostolaki,[a] Elias Sakellis,[ab] Spiros Gardelis[a] and Vlassis Likodimos *[a]

Received 3rd October 2024,
Accepted 4th December 2024

DOI: 10.1039/d4ma00995a

rsc.li/materials-advances

The utilization of hybrid plasmonic metal/semiconductor materials for surface-enhanced Raman scattering (SERS) has emerged as a promising approach towards the development of advanced SERS substrates in terms of sensitivity, uniformity, stability, and reusability, based on the synergy of the powerful electromagnetic mechanism with the chemical amplification and functionality of semiconductor supports. In this work, co-assembled WO_3/TiO_2 inverse opal films were utilized as photonic crystal scaffolds of plasmonic Ag nanoparticles in order to optimally combine plasmonic, charge transfer and slow photon effects for ultrasensitive, recyclable SERS sensing. Compositional and photonic band gap engineering of the Ag-decorated WO_3/TiO_2 photonic crystal substrates provided insight to the interplay of plasmonic enhancement assisted by slow light propagation in the inverse opal structure and charge transfer between the analyte and the heterostructured substrate. Highly sensitive detection of 4-mercaptobenzoic acid as a non-resonant analyte was achieved down to 10^{-13} M for the optimal Ag–WO_3/TiO_2 substrate with good uniformity and excellent recyclability due to its enhanced photocatalytic self-cleaning capacity. Comparative performance tests along with photoelectrochemical evaluation showed a significant contribution of cascade electron transfer from plasmonic Ag to the staggered WO_3/TiO_2 heterojunctions and the analyte, providing an additional charge transfer pathway to promote the substrate-to-molecule interaction for the design of efficient and versatile metal/metal oxide SERS platforms.

1. Introduction

Fueled by the progress of nanotechnology, surface-enhanced Raman scattering (SERS) has evolved from a niche spectroscopic technique to a highly sensitive analytical method offering unparalleled resolution in identifying minute quantities of analytes with great prospects in fundamental research[1] and sensing applications in various fields ranging from food safety[2,3] and environmental monitoring,[4,5] to bioanalysis and disease diagnosis.[6,7] Ultrasensitive SERS detection relies primarily on the marked electromagnetic (EM) enhancement of the inherently weak Raman (inelastic) scattering cross-section of target molecules by the enormous near-field enhancement caused by the excitation of localized surface plasmon resonance (LSPR) modes on nanostructured metallic substrates, especially at asperities or nanoscale gaps (hot spots) between metallic nanoparticles (NPs) along with the concomitant amplification of the emitted radiation.[8] The corresponding enhancement factors (E_Fs) can reach approximately 10^6 in the proximity of an individual plasmonic NP and 10^{10}–10^{11} in the nanometer-sized gap between adjacent NPs (hot spot).[9] The prominent EM amplification is further assisted by a minor contribution ($E_F \sim 10^2$) arising from the analyte-dependent chemical (CM) enhancement *via* the modification of the molecule's polarizability upon adsorption to the substrate surface, enabling molecular-level detection.[10] This unique sensitivity on the identification of target analytes by their Raman spectroscopic fingerprint, which underpinned SERS's application potential,

---

[a] *Section of Condensed Matter Physics, Department of Physics, National and Kapodistrian University of Athens, University Campus, 15784 Athens, Greece. E-mail: vlikodimos@phys.uoa.gr*

[b] *Institute of Nanoscience and Nanotechnology, National Center for Scientific Research "Demokritos", Agia Paraskevi, 15341 Athens, Greece*

† Electronic supplementary information (ESI) available: Absorbance spectra of 4-MBA solution. SEM images of PC films. Kubelka–Munk plots for the WO_3/TiO_2 PC films before and after Ag-deposition. Absorbance spectra of Ag NPs dispersion. Raman spectra of 4-MBA powder and solution on the Ag-PC287 4 : 1. Enhanced Raman scattering for TiO_2 PC287 and PC300 films. Intensity ratio of the non-totally to the totally symmetric mode of 4-MBA and charge transfer degree. Raman intensity of the 1079 and 1585 cm^{-1} modes as a function of 4-MBA concentration. Raman spectra of GSH, R6G and MB analytes and SERS spectra for GSH. Structural and optical properties of Ag–WO_3/TiO_2 PC substrates. See DOI: **https://doi.org/10.1039/d4ma00995a**

simultaneously poses a significant challenge in the reproducibility of metallic SERS substrates with uniform hot spot spatial distributions.[11] The strongly intensified local fields are also responsible for the perturbative nature of the technique, which may induce adverse photochemical, thermal or photothermal reactions in the molecule–substrate system.[12]

Semiconductor-based enhanced Raman scattering has recently emerged as a promising alternative and/or complementary approach to metal-based SERS detection, providing distinct advantages such as low invasiveness, enhanced chemical stability and reproducibility, versatility, and recyclability.[11–13] An upsurge of research has been witnessed in recent years on the development of plasmon-free, semiconductor SERS substrates, where the amplification of Raman scattering has been primarily associated with the CM mechanism, involving interfacial electron transfer between the analyte and the semiconducting substrate, which, in conjunction with exciton and molecular resonances, may lead to E_Fs up to 10^6 under optimal conditions.[14,15] Semiconductor SERS can be greatly assisted by the formation of molecular charge transfer complexes that enhance the molecule–substrate vibronic coupling.[16] Charge transfer in molecule–semiconductor SERS systems can be enhanced *via* defect engineering as reported for non-stoichiometric WO_3,[17,18] Cu_2O,[19] ZnO[20] and TiO_2[21] metal oxide substrates, while the formation of type II semiconductor heterojunctions has been recently pursued for MoO_x/WO_x[22] and ZnO/TiO_2[23] as an advanced approach to improve SERS performance *via* charge transfer. Although significantly high E_Fs have been achieved, the inherent specificity of charge transfer-based SERS that depends on the coupling between the excitation laser wavelength and the energy levels of the molecule–substrate system[24] limits the applicability of semiconductor SERS substrates in comparison to the universal plasmonic enhancement catered by conventional metal SERS sensors.

Given the limitations of single-enhancement SERS mechanisms, implementation of cooperative resonance effects was recently set forth as a potent approach to improve the performance of semiconductor substrates. Highly sensitive SERS detection of dye molecules has been reported for Cu_2O spheres of tunable concavity based on the synergy of CM mechanism with the enhanced light trapping in the spherical cavities,[25] while the synergy of Mie resonances and charge transfer was achieved by adjusting the diameter of spherical ZnO superstructures for the SERS detection of non-resonant analyte molecules.[26] The combination of multiple resonances was further shown by tuning the dye analyte's molecular resonance to the photo-induced charge transfer and EM enhancement in band-gap-engineered Ta_2O_5 nanorods[27] as well as double-shell hollow spherical V_2O_5 microstructures[28] corroborating that judicious shape engineering may drastically increase the optical path length and sensitivity in semiconductor SERS substrates. Among different morphologies, photonic crystals (PCs) in the form of bottom-up assembled inverse opals have attracted particular attention as an advanced platform to enable spectrally selective EM enhancement in semiconductor SERS by slow photon effects, *i.e.*, light propagation at reduced group velocity near the edges of the photonic band gap (PBG), which may extend the path length of incident light at the corresponding wavelengths within the periodically structured network.[29] Tuning the slow photon region to the laser excitation has been shown to significantly enhance SERS detection of dye molecules in PBG-engineered TiO_2 inverse opal substrates,[30] especially after combination with the CM enhancement provided by the high adsorption capacity and surface reactivity of graphene oxide nanosheets grafted on the nanocrystalline walls of TiO_2 inverse opals.[31] Furthermore, inverse opal SERS substrates can be exploited as ideal scaffolds to load plasmonic NPs at high densities leading to hybrid plasmonic metal/semiconductor SERS platforms that combine the powerful EM-enhanced sensitivity of noble metal LSPR with the CM amplification and functionality of semiconductor supports.[3,32,33]

In this work, heterostructured PBG engineered Ag–WO_3/TiO_2 inverse opal films are demonstrated as ultrasensitive, recyclable SERS sensors based on the optimal combination of plasmonic, charge transfer, and slow photon effects. Bottom-up three-phase co-assembly has been applied for the concurrent crystallization of WO_3 and TiO_2 into a single interconnected PC structure comprising a broad distribution of nanoscale heterojunctions between the two metal oxides, which was post-decorated by plasmonic Ag NPs. Compositional WO_3/TiO_2 alloying along with the variation of the templating sphere diameter allowed investigating the interplay of EM enhancement from the Ag LSPR with slow photon tuning and the CM mechanism *via* the interfacial charge transfer between the probe molecules and the plasmonic-metal oxide substrate. Ultrasensitive detection of 4-mercaptobenzoic acid (4-MBA) as non-resonant analyte has been achieved down to 10^{-13} M for the optimal hybrid plasmonic-photonic Ag–WO_3/TiO_2 substrate with very good uniformity and excellent self-cleaning performance and reusability. A significant CM contribution was concluded *via* cascade electron transfer from the plasmonic NPs to the metal oxide substrate and the 4-MBA molecules, where heterojunction WO_3/TiO_2 formation was crucial to the markedly enhanced SERS performance by offering an efficient charge transfer route to enhance charge separation and the substrate-to-molecule interaction.

2. Experimental

2.1 Ag–WO_3/TiO_2 inverse opal substrate fabrication

Single and composite WO_3/TiO_2 inverse opal films were deposited on glass substrates using the convective evaporative co-assembly method of polymer templating spheres of different diameters in the form of aqueous colloidal dispersions with the corresponding hydrolyzed metal oxide precursors.[34] Specifically, monodisperse polystyrene (PS) spheres with mean diameters of 287, 300 and 340 nm and poly(methyl methacrylate) (PMMA) ones of 406 nm diameter, which were obtained from Microparticles GmbH in the form of colloidal dispersions of 5% solids (w/v) in deionized water (6–10 nm standard deviation and 2.4–3.5% CV), were used as hard templates. The WO_3 precursor was prepared by dissolving 0.2 g ammonium metatungstate hydrate (AMT) $(NH_4)_6W_{12}O_{39}\cdot xH_2O$ (Alfa Aesar) powder in 1 mL H_2O, 0.12 mL of 0.1 M citric acid ($\geq$99.5%, Alfa

Aesar) and 0.6 mL EtOH (absolute ≥99.8%, Honeywell Riedel-de Haën), while the TiO_2 precursor was prepared by mixing 0.25 mL of 50 wt% aqueous solution of Ti(IV) bis(ammonium lactato) dihydroxide (TiBALDH) from Alfa Aesar with 0.5 mL of 0.1 M HCl (fuming, ≥37%) and 1 mL EtOH. Typically, a glass slide, cleaned by Hellmanex^{TM} III (Sigma Aldrich) and ultrasound sonication in acetone and EtOH, was almost vertically suspended in a beaker containing 8 mL of 0.125 wt% polymer sphere suspension and 0.05 mL of single or mixed AMT/TiBALDH precursor at nominal molar W/Ti ratios of 4 : 1 and 1 : 2. After solvent evaporation at 55 °C, the co-assembled films were calcined in air at 450 °C for 2 h at 1 °C min^{-1} heating rate to remove the polymer spheres and crystallize the metal oxides in the inverse opal structure. The inverse opal films were then surface modified with Ag NPs (Thermo Scientific, 10 nm mean diameter, 0.02 mg mL^{-1} suspension, supplied in 2 mM sodium citrate, 4×10^{12} NP mL^{-1}) by dropping 40 μL of the suspension on the substrates' surface (0.5 cm^2), followed by drying and washing with DI water and ethanol (Scheme 1). The PC films were labelled as Ag-PCXXX Y : Y, with XXX being the templating sphere diameter (287, 300, 340 and 406 nm) and Y : Y the W/Ti ratio (4 : 1 or 1 : 2).

2.2 Materials characterization

The films morphology and phase composition were studied using a FEI Quanta Inspect scanning electron microscope (SEM) equipped with an energy-dispersive X-ray analyzer (EDX) and a FEI Talos F200i scanning transmission electron microscope (TEM) operating at 200 keV, equipped with a windowless energy-dispersive spectroscopy microanalyzer (6 T/100 Bruker). The optical properties were investigated by specular (*R*%) and diffuse (DR%) reflectance measurements on a Cary 60 UV-vis spectrometer equipped with a 15° specular reflectance accessory and fiber-optic diffuse reflectance, using a UV-enhanced Al mirror and a Halon reference for background determination, respectively. Electrochemical impedance spectroscopy (EIS) was carried out in a standard three-electrode configuration on a CS350 potentiostat/galvanostat (Corrtest Instruments) using the Ag–WO_3/TiO_2 PC films deposited on fluorine-doped tin oxide (FTO, thickness 2.2 mm, surface resistivity 7 Ω sq^{-1}) glass substrates as working electrodes, Ag/AgCl as reference and a Pt foil as counter electrodes in aqueous 0.1 M $NaHCO_3$ electrolyte under UV-vis illumination provided by a 300 W Xe lamp (100 mW cm^{-2}). Nyquist plots were performed in the frequency range of 10^5–10^{-2} Hz with ac amplitude of 10 mV, while Mott–Schottky curves were derived from the electrochemical impedance at 500 Hz. The applied potential *vs.* reference electrode was converted to the reversible hydrogen electrode (RHE) scale using Nernst equation: $V_{RHE} = V_{Ag/AgCl} + 0.059\ pH + 0.205$.

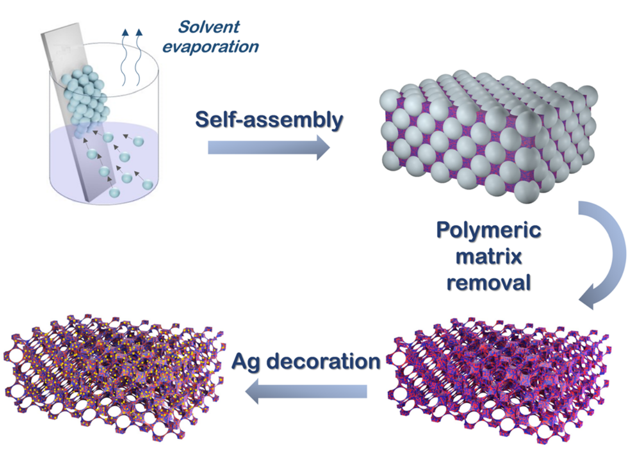

Scheme 1 Schematic of the co-assembly fabrication of Ag–WO_3/TiO_2 inverse opals.

2.3 SERS performance evaluation

The SERS performance of the PC substrates was evaluated on the detection of 4-mercaptobenzoic acid (4-MBA) as a model, non-resonant analyte,[35] which shows absorption in UV range (Fig. S1, ESI†) avoiding resonant excitation under visible light lasers. Additional validation tests were performed on rhodamine 6G (R6G) and methylene blue (MB) dye analytes and glutathione (GSH). 4-MBA (99%, Sigma Aldrich), R6G (99%, Sigma Aldrich) and MB (≥96.0 to ≤104.0%, Thermo Scientific) powders were dissolved in EtOH to prepare solutions of variable concentrations in the range of 10^{-4} to 10^{-13} M, while GSH (≥98.0%, Sigma-Aldrich) was dissolved in DI water. These solutions were dropped onto the inverse opal substrates and dried at room temperature. Micro-Raman spectra were collected on a EnSpectr RamMics M532 Raman spectrometer coupled with a BX43 Olympus microscope using a 532 nm laser diode as excitation source, focused on the film surface by a 40× (NA = 0.65) objective. The Raman spectra were averaged over at least five different spots for each film with accumulation time of 2 s, while frequency shifts were calibrated by a Si reference.

Raman maps were acquired using a LabRAM Soleil Horiba Raman microscope with 532 nm laser excitation, focused by a 100× (NA = 0.9) objective, while a laser diode emitting at 785 nm was used as excitation for the GSH SERS spectra.

3. Results and discussion

3.1 Structural and compositional properties

The PC substrates display the characteristic inverse opal structure consisting of hexagonally ordered macropores, as shown by the top-view and cross-section SEM images in Fig. 1 and Fig. S2 (ESI†). Co-assembly of the AMT and TiBALDH precursors with templating spheres of different diameters resulted in well-ordered periodic structures with thickness of *circa* 4.7(1) μm, independent of the W/Ti molar ratio and the Ag NPs surface modification. Smaller pores were present in the walls of every macropore derived from the contact points between the polymer spheres, verifying the formation of uniformly interconnected networks that provide ideal platforms for post-modification by Ag NPs and enhanced adsorption of analytes. The mean diameter of the spherical voids and thus the lattice constant of the close-packed structure was determined by both

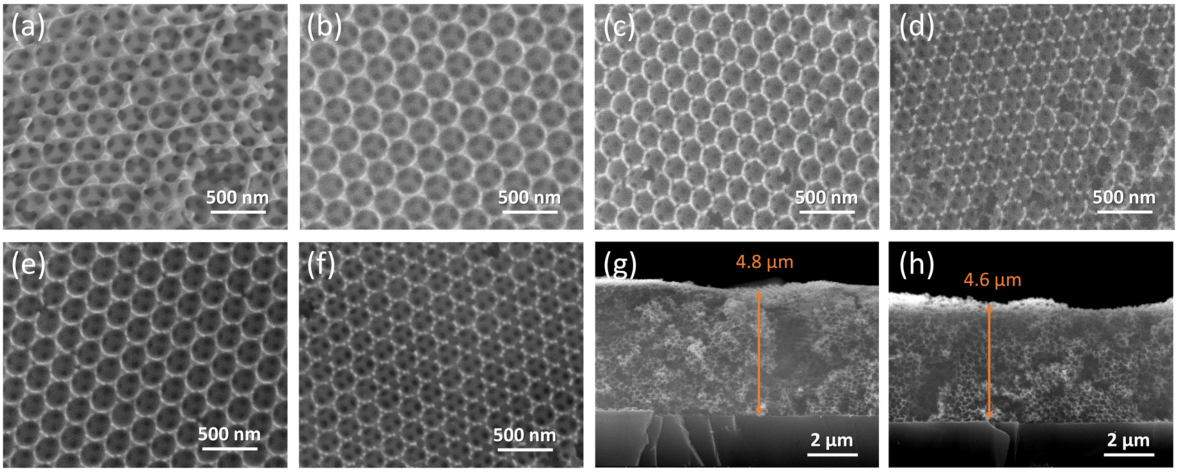

Fig. 1 Top-view SEM images for PC287 (a) WO_3, (b) 4 : 1, (c) 1 : 2, (d) TiO_2 as well as (e) Ag-PC287 4 : 1, and (f) Ag-PC287 1 : 2 substrates. Cross-section SEM images for PC287 (g) 4 : 1 and (h) 1 : 2 films.

the size of the sacrificial polymer spheres and the W/Ti composition (Table S1, ESI†). Increase of the W/Ti ratio led to the increase of macropore size for the same templating sphere diameter, stemming from the relatively faster crystallization of WO_3 NPs by the AMT precursor[36] compared to that of TiO_2 nanocrystallites by TiBALDH co-assembly in the inverse opal skeleton.[37] Compositional alloying of the inverse opal concurrently with PBG engineering could be accordingly performed allowing the investigation of interfacial charge transfer effects for PC substrates of similar periodicity.

TEM images of the Ag-PC287 4 : 1 PC film and the corresponding W, Ti, O and Ag EDX elemental maps revealed the uniform distribution of the two metal oxides throughout the inverse opal skeleton and dense coverage by Ag NPs, as shown in Fig. 2a–e. High-resolution TEM (HRTEM) images of the skeletal walls confirmed the presence of spherical NPs (Fig. 2g) with lattice fringes corresponding to about 2.36 Å interplanar spacing assigned to the (111) crystal planes of Ag fcc lattice.

The phase composition of the WO_3/TiO_2 PCs was investigated by Raman spectroscopy and high-resolution TEM, as shown in Fig. 3. Raman spectra of the plain TiO_2 PC films showed the characteristic vibrations of the anatase TiO_2 phase, namely the E_g modes at 152, 199, and 641 cm^{-1} and the B_{1g} and $A_{1g} + B_{1g}$ ones at 398 and 517 cm^{-1}, respectively, independent of the macropore diameter (Fig. 3a and b). The anatase Raman modes showed appreciable broadening and frequency shifts compared to the bulk values, indicative of the breakdown of the

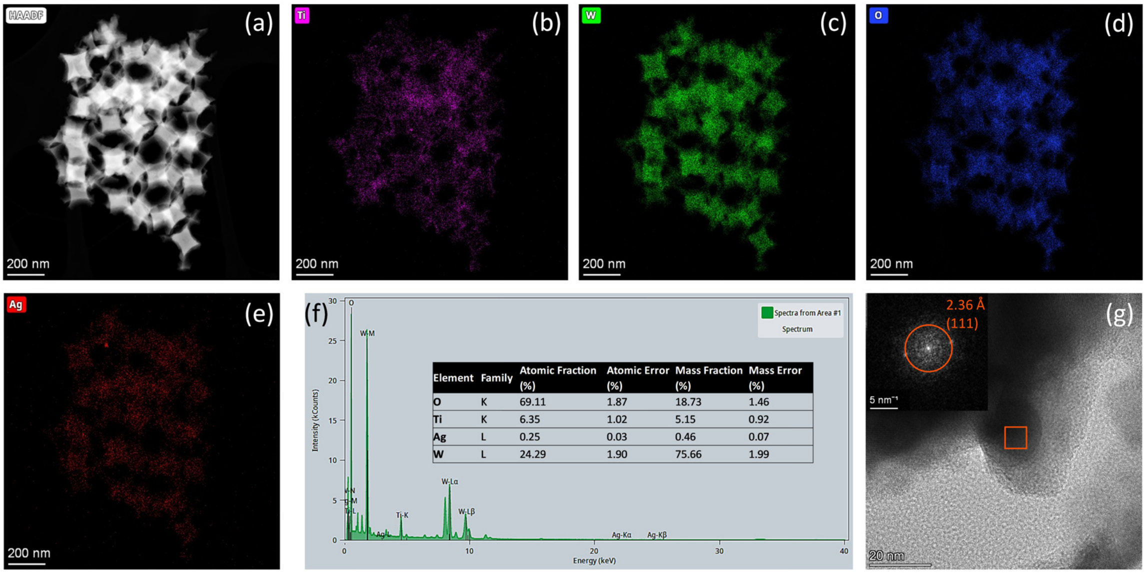

Element	Family	Atomic Fraction (%)	Atomic Error (%)	Mass Fraction (%)	Mass Error (%)
O	K	69.11	1.87	18.73	1.46
Ti	K	6.35	1.02	5.15	0.92
Ag	L	0.25	0.03	0.46	0.07
W	L	24.29	1.90	75.66	1.99

Fig. 2 (a) TEM image of Ag-PC287 4 : 1 film and the (b) Ti, (c) W, (d) O and (e) Ag elemental maps obtained from the corresponding (f) EDX spectrum (g) high-resolution TEM image and the corresponding FFT pattern for the squared area over a relatively isolated NP identifying the (111) planes of Ag (fcc) with 2.36 Å interplanar spacing.

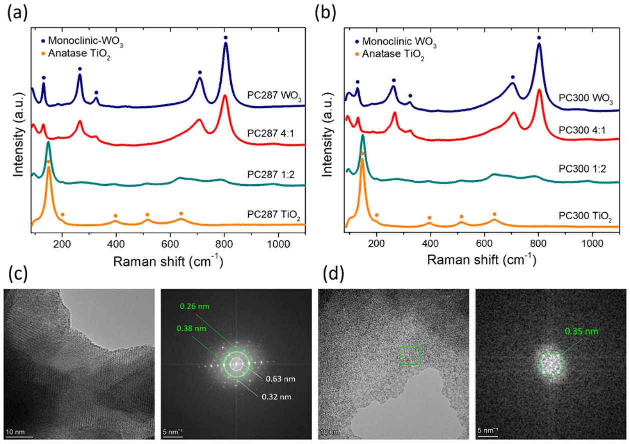

Fig. 3 Raman spectra for the (a) PC287 and (b) PC300 WO_3/TiO_2 substrates at 532 nm. High resolution TEM images for (c) the plain PC287 WO_3 and (d) PC287 1 : 2 films and the corresponding FFT patterns for the whole TEM image in (c) and the squared area in (d).

$q = 0$ selection rule for Raman scattering due to size effects.[38] This complies with previous results for co-assembled TiO_2 inverse opals using the TiBALDH precursor that hinders particle growth within the interstitial space between templating spheres.[39] The correlation curves of frequency *vs.* full-width at half-maximum (FWHM) of the most intense E_g mode[38] indicate the formation of *ca.* 6 nm anatase NPs. Co-assembly of TiBALDH with the AMT precursor resulted in the marked attenuation and further broadening of the anatase Raman bands for 1 : 2 molar W/Ti ratio, while they could not be detected for the 4 : 1 mixed composition. For the plain WO_3 PC films, the characteristic modes of the monoclinic WO_3 phase (ms-WO_3) were observed at 805, 709 (W–O–W stretching), 325, 264 (W–O–W bending), and 131 (lattice modes) cm^{-1},[40] along with a band at about 950 cm^{-1} and a broad shoulder at about 640 cm^{-1} related to the W=O stretching vibration mode in tungsten trioxide hydrates.[41] Significant broadening of the WO_3 Raman bands was observed for the 4 : 1 WO_3/TiO_2 PCs indicating the decrease of crystallite size along with the increase of W^{5+} defect concentration.[34]

This behaviour was corroborated by high-resolution TEM analysis, as shown in Fig. 3c and d. Clear lattice fringes were observed for the plain PC287 WO_3 (Fig. 3c) leading to strong diffraction spots in the corresponding FFT pattern, supporting the growth of well-developed WO_3 crystallites. Specifically, the derived interplanar spacings of 0.26 and 0.38 nm could be identified with the closely spaced (002), (020), (200) and (202), $(\bar{2}02)$, (022) groups of crystal planes of the ms-WO_3 phase (JCPDS 43-1035), while the 0.32 and 0.63 nm spacings resulted from the (220), (040) and (020) planes of the hydrated $WO_3\cdot0.33H_2O$ orthorhombic phase (JCPDS 35-0270). On the other hand, sub-10 nm NPs were detected for the PC287 1 : 2 films (Fig. 3c), the most common being those exhibiting diffraction from the (101) planes of anatase NPs with 0.35 nm interplanar spacing (JCPDS 21-1272). The competition of TiBALDH and AMT precursors can be accordingly considered to impede the growth of the metal oxide NPs, which along with the accompanying defect formation can be beneficial to the SERS performance *via* charge transfer effects.

3.2 Optical properties

Specular reflectance spectra (R%) of the TiO_2, WO_3 and composite WO_3/TiO_2 PC films at 15° incident angle showed a distinct peak due to Bragg reflection, characteristic of the incomplete PBG (stop band) formation along the [111] direction in the inverse opals,[42] as shown in Fig. 4a–c. The stop band position shifted to longer wavelengths as either the templating sphere diameter or the W/Ti molar ratio increase following the corresponding macropore size variation. Applying modified Bragg's law for first-order diffraction from the (111) planes of the fcc lattice and using the experimental stop band wavelengths and the measured macropore diameter D, the PBG position at normal incidence (0°) and the values of the effective refractive index n_{eff} were estimated for the PC films (Table S1, ESI†). The derived solid filling fractions $(1 - f)$ were smaller than the theoretical value of 0.26 for complete filling of the fcc interstitial space and decreased with the increase of polymer sphere diameter and the decrease of the compositional W/Ti ratio. This can be related with the enhanced mesoporosity of the skeletal walls by increasing the number of interfaces for smaller macropores and the formation of sub-10 nm NPs in the inverse opal frame, especially for the TiO_2 PCs.[37]

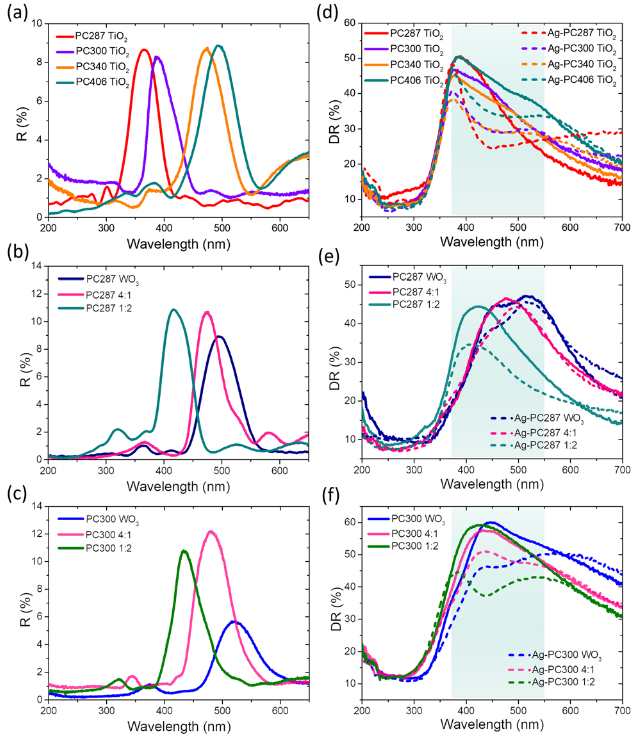

Fig. 4 (a)–(c) Specular reflectance R% spectra showing the Bragg reflection for the WO_3/TiO_2 PC films. (d)–(f) Diffuse reflectance DR% spectra for the WO_3/TiO_2 (solid lines) and Ag–WO_3/TiO_2 (dashed lines) PC substrates. The cyan band delineates the spectral region of plasmonic Ag NP absorption on the metal oxide films.

The diffuse reflectance (DR%) spectra of the single WO_3 and TiO_2 PC films (Fig. 4d–f) were mainly determined by the absorption edges of the metal oxides, which were estimated at 450 and 370 nm from the corresponding absorbance spectra obtained by the Kubelka–Munk remission function F(DR) (Fig. S3, ESI†). Rather broad Bragg reflections could be identified in the DR % spectra, red-shifted from the corresponding *R*% peaks due to the increased scattering at the low energy (red) stop band edges,[39] only for the larger diameter-PCs, where spectral overlap of the stop band and the semiconductor electronic bandgap was marginal, evading absorption losses. The superposition of the metal oxide absorption edges could be distinguished in the case of the WO_3/TiO_2 PC 4 : 1 films, whereas the contribution of TiO_2 prevailed in the DR% spectra of the WO_3/TiO_2 PC 1 : 2. Surface modification of the WO_3/TiO_2 PC films with plasmonic Ag NPs resulted in the marked drop of DR%, which extended up to *ca.* 550 nm, beyond the much narrower LSPR of the Ag NPs dispersion (Fig. S4, ESI†). This can be associated with the red-shift of the Ag NP LSPR absorption due to near-field coupling between closely spaced plasmonic NPs leading to hot spots and marked enhancement of the local field.[43,44] The extent of DR% reduction after Ag NP deposition was most pronounced for the smaller diameter PCs, such as the Ag-modified PC287 and PC300 TiO_2 (Fig. 4d), PC287 1 : 2 (Fig. 4e) and PC300 1 : 2 (Fig. 4f), where higher amounts of Ag NP aggregates and enhanced hot spot formation can be expected.

3.3 SERS evaluation

The SERS activity of the inverse opal substrates was evaluated on 4-MBA detection as a non-resonant probe molecule, whose absorbance at the UV range (Fig. S1, ESI†) precludes resonance Raman excitation at 532 nm. Fig. 5 and 6 show SERS spectra of 4-MBA adsorbed on Ag–TiO_2 as well as Ag–WO_3 and Ag–WO_3/TiO_2 PC substrates of different void diameters as a function of the analyte concentration to the lowest detectable level. The characteristic 4-MBA vibrations were readily detected on Ag–WO_3/TiO_2 PC films though considerably shifted compared to the corresponding powder Raman spectrum (Fig. S5, ESI†), as a result of the bonding of 4-MBA molecules to the metal oxides and Ag NPs *via* the thiol and/or carboxyl groups.[16,45] The dominant 4-MBA bands were observed at 1079 (ν_{12}, a_1) and 1585 (ν_{9a}, a_1) cm^{-1}, arising from the aromatic ring vibrations, while those at 1140 (ν_{15}, b_2) and 1182 (ν_9, a_1) cm^{-1} correspond to the C–H deformation modes (Table 1).[46] Monitoring of 4-MBA down to the lowest detectable concentration has been accordingly carried out using the strongest Raman bands at 1079 and 1585 cm^{-1}, whose relative intensity remained approximately constant.

In the case of PBG engineered Ag–TiO_2 PCs, 4-MBA could be traced down to very low concentrations with the Ag–TiO_2 PC287 substrates of the smallest macropore size presenting the lowest detectable level of 10^{-12} M (Fig. 5a). As the corresponding PBG at 375 nm (Table S1, ESI†) is well below the Raman excitation wavelength (532 nm), this high sensitivity in 4-MBA detection can be largely related to the EM enhancement afforded by the Ag NPs LSPR.[47] The latter can be combined with the CM amplification at the 4-MBA/Ag–TiO_2 interface, which proceeds by the photoinduced TiO_2-to-4-MBA charge transfer *via* surface states, further assisted by hot-electron transfer to the anatase conduction band over the corresponding Schottky barrier at the metal-semiconductor heterojunction.[45] The LSPR amplification is expected to be most prominent for the Ag–TiO_2 PC287 substrates that exhibit the higher solid filling faction of its nanocrystalline anatase skeleton (Table S1, ESI†) and thus enables higher loading of Ag NPs and the possibility of the formation of more hot spots, in accordance with the highest and more extended visible light absorption due to Ag LSPR among the Ag–TiO_2 PCs (Fig. 4d and Fig. S3a, ESI†). Charge transfer can be also promoted in the case of co-assembled Ag–TiO_2 PCs using the TiBALDH precursor by the growth of very small, sub-10 nm, anatase NPs in the inverse opal skeleton, which are most susceptible to the formation of surface states that mediate electron transfer from TiO_2 to the lowest unoccupied molecular orbital (LUMO) of the adsorbed 4-MBA molecules.[46,48] The increase of macropore size for Ag–TiO_2 PC300 leads to significant drop of SERS performance (the lowest detectable concentration of 4-MBA is 10^{-9} M) (Fig. 5b) that can be associated with the decrease of Ag plasmonic absorption (Fig. S3a, ESI†) due to the lower Ag NP loading that follows the decrease of the corresponding filling fraction (Table S1, ESI†). This could be further related to the enhancement of the anatase Raman mode intensity for the Ag–TiO_2 PC287 films (Fig. S6, ESI†), which arise from SERS effects at the

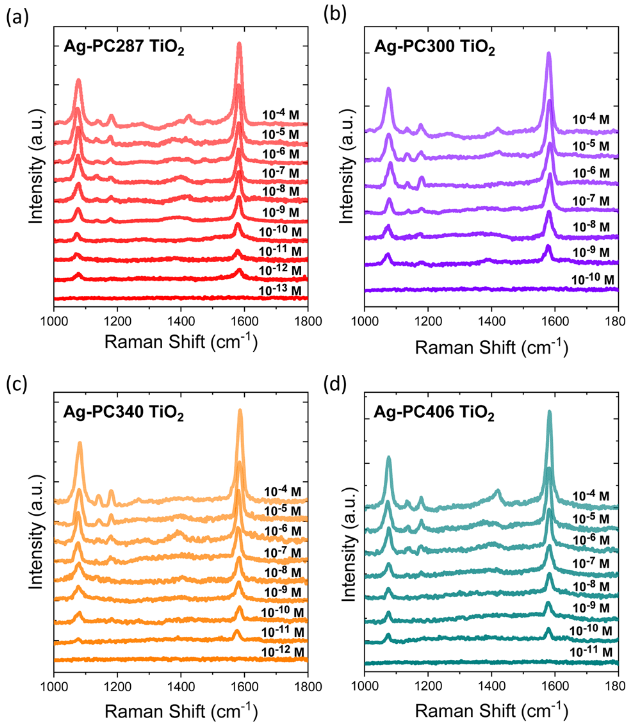

Fig. 5 SERS spectra of 4-MBA of variable concentrations (10^{-4}–10^{-13} M) on Ag–TiO_2 (a) PC287, (b) PC300, (c) PC340 and (d) PC406 inverse opal substrates of different macropore diameter and PBG.

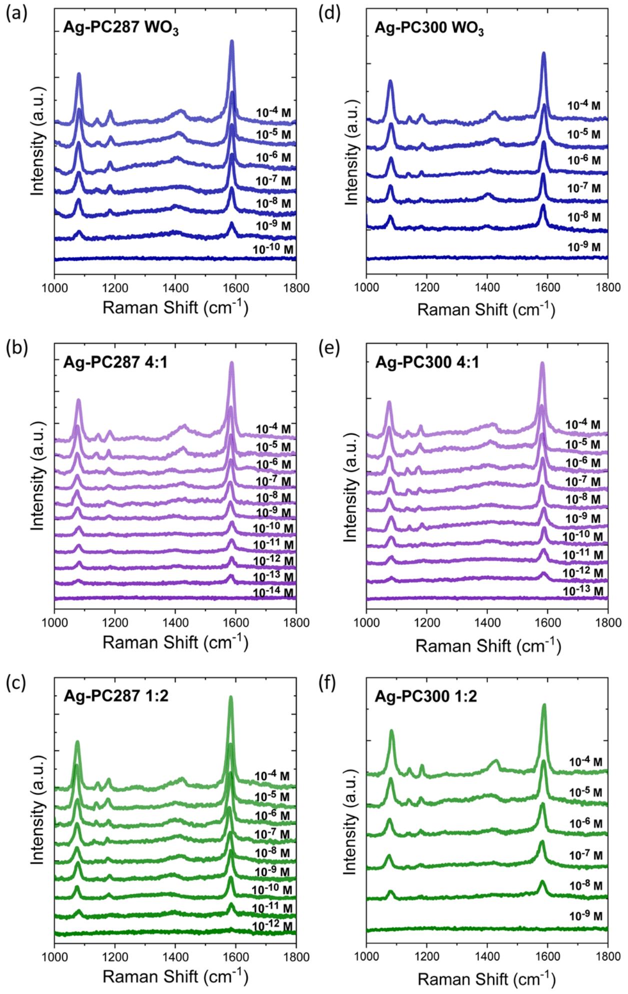

Fig. 6 SERS spectra of 4-MBA as a function of concentration (10^{-4}–10^{-13} M) on (a) Ag-PC287 WO$_3$, (b) Ag-PC287 4:1, (c) Ag-PC287 1:2, (d) Ag-PC300 WO$_3$, (e) Ag-PC300 4:1 and (f) Ag-PC300 1:2 inverse opal substrates of variable macropore size and composition.

Table 1 Vibrational frequencies of selected 4-MBA Raman modes on Ag–WO$_3$/TiO$_2$ PC substrates compared to solid powder and band assignments[46]

4-MBA powder (cm^{-1})	Ag–WO$_3$/TiO$_2$ PCs (cm^{-1})	Band assignment
1095	1079	Ring breathing
1133	1140	CH bending
1179	1182	CH bending
1450	1420	COO$^-$ stretching
1592	1585	Ring breathing

semiconductor-plasmonic NP interface, especially near hot spots, as reported for TiO$_2$/Au films[49] and very recently for MoS$_2$/Ag NP hybrids.[50] The enhancement of TiO$_2$ Raman intensity was also observed for the Ag–TiO$_2$ PC300, though weaker than the corresponding PC287 films, corroborating the decrease of Ag NP loading in the inverse opal skeleton for larger macropores.

Furthermore, significant improvement of 4-MBA SERS detection reaching 10^{-11} M was observed for the Ag–TiO$_2$ PC340 substrates (Fig. 5c), which show smaller $1 - f$ values and similar plasmonic absorption compared to Ag–TiO$_2$ PC300 (Fig. S3a, ESI†). This performance recovery can be related to the contribution of slow light propagation as the incident laser excitation approaches the low-energy (red) edge of the PC340 stop band. Assuming that the PBG spectral width corresponds to the corresponding FWHM of about 60 nm of the Bragg R% reflection (Fig. 4a), the stop band for Ag–TiO$_2$ PC340 is expected at 483 ± 30 nm (Table S1, ESI†). The corresponding red-edge slow photons, which extend over a narrower spectral range of *ca.* 20 nm,[31] will be then expected at 513–533 nm, approaching the laser wavelength that leads to enhanced light scattering within the inverse opal skeleton and assists 4-MBA detection. Further shift of the PBG at 503 nm for Ag–TiO$_2$ PC406 (Table S1, ESI†) could also lead to photonic amplification of Raman scattering *via* red slow photons anticipated at approximately 533–553 nm. However, the larger macropore diameter of PC406 leads to appreciable decrease of the filling fraction (Table S1, ESI†) and the lowest plasmonic absorption (Fig. S3a, ESI†) among the Ag–TiO$_2$ PCs that impede LSPR enhancement by Ag NPs and finally lead to the decrease of SERS sensitivity to 10^{-10} M (Fig. 5d).

For the plain Ag–WO$_3$ PC substrates the SERS performance was considerably moderated in comparison to the Ag–TiO$_2$ PCs (Fig. 6a and d), despite the relatively higher filling fractions of the WO$_3$ inverse opal skeleton (Table S1, ESI†). The LSPR-induced plasmonic absorption for the Ag–WO$_3$ PCs was also weaker (Fig. S3b and c, ESI†) indicating that the larger $1 - f$ values resulted mainly from the growth of larger crystallites and the reduced wall mesoporosity of the WO$_3$ inverse opals. Still, the Ag–WO$_3$ PC287 substrates (Fig. 6a) outperformed Ag–WO$_3$ PC300 (Fig. 6d), reaching 10^{-9} M as the lowest 4-MBA detectable concentration, indicative of the contribution of photonic amplification in the overall SERS enhancement. In fact, the stop band for the Ag–WO$_3$ PC287 occurs at 504 ± 30 nm (Table S1, ESI†), whose low energy (red) edge may extend roughly at 534–554 nm, close to the laser excitation wavelength that may enhance Raman scattering and SERS performance. On the other hand, the stop band of the larger diameter Ag–WO$_3$ PC300 is expected in the spectral range 495–555 nm, matching the laser excitation that could lead to detrimental Bragg reflection and partially inhibit light propagation in the inverse opal structure. However, compositing WO$_3$ PCs with TiO$_2$ resulted in marked amplification of SERS performance, in agreement with preliminary SERS results on the WO$_3$/TiO$_2$ PC287 substrates.[51] The SERS sensitivity reached the lowest 4-MBA detectable levels of 10^{-13} and 10^{-12} M for the Ag-PC287 4:1 (Fig. 6b) and Ag-PC300 4:1 (Fig. 6e) substrates, respectively. This variation indicates a major contribution of the CM mechanism *via* interfacial charge transfer between the two metal oxide semiconductors by the formation of type II heterojunctions.[23,52] The PBG positions of the two composite Ag–WO$_3$/TiO$_2$ PC287 and PC300 substrates were at 485 and 498 nm (Table S1, ESI†). This enabled spectral matching of red slow photons with the laser wavelength, similar to the plain Ag-PC340 substrate, which, however, showed considerably lower sensitivity (10^{-11} M) (Fig. 5c), corroborating the contribution of enhanced charge transfer in the heterostructured substrate. Further decrease of the W/Ti ratio to 1 : 2 resulted in the deterioration of SERS performance (Fig. 6c and f), especially for the larger diameter Ag-PC300 1 : 2 that presented similar 4-MBA detection levels as the parent Ag-PC300, indicative of a non-optimal composition.

In order to investigate interfacial charge transfer in the Ag–WO_3/TiO_2 system, comparative EIS measurements were performed on the best-performing PC287 TiO_2 and PC287 4 : 1 substrates, before and after Ag NPs deposition, under UV-Vis illumination (Fig. 7). Nyquist plots for the unmodified PC287 films showed significant decrease of the capacitive arc radius (Fig. 7a), which represents the charge transfer resistance at the semiconductor–electrolyte, for the composite PC287 4 : 1 substrate. This verifies the enhanced separation of photo-induced charge carriers *via* the formation of nanoscale WO_3-TiO_2 heterojunctions and the ensuing electron transfer from WO_3 to the TiO_2 NPs, recently established for co-assembled WO_3/TiO_2 PCs.[34] Moreover, Ag deposition resulted in further reduction of charge transfer resistance for both Ag-PC287 TiO_2 and Ag-PC287 4 : 1 films, indicative of additional contributions by plasmonic NPs in the underlying charge transfer process. The corresponding Mott–Schottky (MS) plots, *i.e.* $1/C^2$ *vs.* applied potential with C being the space-charge capacitance, showed positive slopes confirming the n-type semiconducting of both WO_3 and TiO_2 metal oxides (Fig. 7b). The slope of the linear part of the MS plot was markedly smaller for PC287 4 : 1 indicating higher donor density compared to the plain PC287 TiO_2. Further increase of donor density was derived after deposition of the plasmonic Ag NPs on the metal oxide PCs, supporting the role of Ag NPs in assisting charge transfer at the metal-semiconductor interface.

The contribution of the molecule–substrate charge transfer to the SERS mechanism was further explored using the selective enhancement of non-totally symmetric modes of the probe molecules over symmetric ones by the Herzberg–Teller vibronic coupling.[53] The intensity ratio of the non-totally (1140 cm^{-1}, b_2) to the totally (1182 cm^{-1}, a_1) symmetric mode of 4-MBA was accordingly selected to monitor the variation of charge transfer contribution to SERS enhancement for the Ag-PC287 substrates (Fig. S7a, ESI†). The values of the $I(b_2)/I(a_1)$ ratio showed a clear enhancement of the non-totally symmetric b_2 mode for the single Ag–TiO_2 and Ag–WO_3 PCs, which was further amplified for the composite Ag–WO_3/TiO_2 PCs. This variation points to the close combination of CM enhancement *via* charge transfer between the molecule and the metal-semiconductor substrate with the plasmonic EM mechanism for the heterostructured Ag–WO_3/TiO_2 PC substrates. A quantitative estimate of the relative CT contribution to the overall SERS intensity was made by calculating the corresponding quantity p_{CT} for the b_2 and a_1 modes, whose values of 0 and 1 indicate the limits of zero and dominant CT contributions, respectively.[53] The obtained values of 0.28(2), 0.33(3), 0.43(2), 0.42(2) for the Ag-modified TiO_2, WO_3, 4 : 1 and 2 : 1 PC287 substrates, respectively (Fig. S7b, ESI†), indicate an increase of the degree of CT for the composite PC substrates, for which comparable contribution of CT to the EM plasmonic amplification is reached.

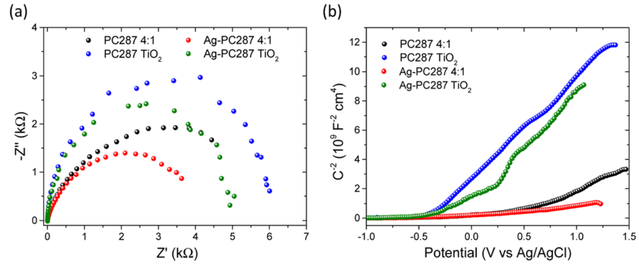

Fig. 7 Comparative (a) Nyquist and (b) Mott–Schottky plots for PC287 4 : 1 and TiO_2 substrates before and after Ag deposition at 500 Hz.

According to these results, ultrasensitive detection of 4-MBA down to 10^{-13} M can be reached on hybrid Ag–WO_3/TiO_2 PC substrates *via* the synergy of plasmonic, charge transfer and slow photon effects. Specifically, EM enhancement proceeds *via* the LSPR of Ag NPs that can be amply loaded on the skeletal walls of metal oxide inverse opals, especially when composed of sub-10 nm NPs as for the co-assembled Ag–TiO_2 PCs. In addition, the plasmonic SERS amplification can be further improved by slow light propagation in the PC skeleton, as evidenced for the PBG engineered Ag–TiO_2 PCs. Although the enhanced SERS performance can be largely attributed to the amplified EM field at the interface of Ag and the metal oxide inverse opal skeleton, interfacial charge transfer plays also a crucial role in the Ag–WO_3/TiO_2-4-MBA system. When the two semiconductors come into contact, their Fermi energy (E_F) levels equilibrate according to the staggered type II band alignment of the WO_3/TiO_2 heterojunction,[34] as shown in Fig. 8. The highest occupied molecular orbital (HOMO) and the LUMO levels of 4-MBA are expected at −8.84 and −3.85 eV,[23] respectively, while the E_F of Ag is located at 4.84 eV (absolute vacuum scale).[54] The laser excitation at 532 nm corresponds to 2.33 eV photon energy, which is

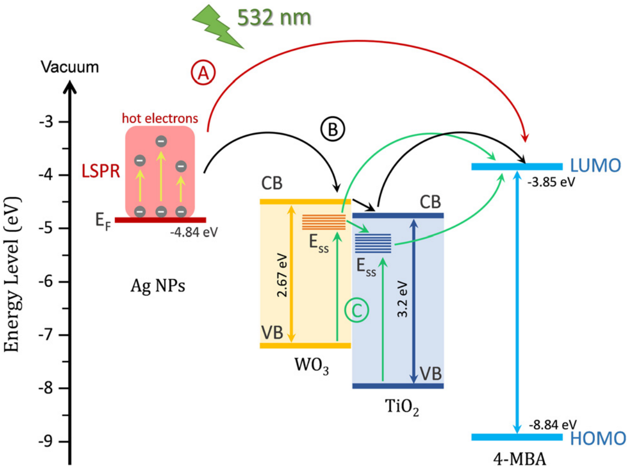

Fig. 8 Proposed charge transfer pathways in the Ag–WO_3/TiO_2 system for 4-MBA SERS detection.

inadequate to excite electrons either from the HOMO to the LUMO of 4-MBA or from the valence band (VB) maximum to the conduction band (CB) minimum in TiO_2 and WO_3, whose E_{CB} and E_{VB} band edges in the WO_3/TiO_2 heterojunction (4 : 1 molar ratio) are estimated at −4.73 and −7.93 eV for TiO_2 and −4.52 and −7.19 eV for WO_3, respectively.[34] Three possible charge transfer processes are accordingly proposed at 532 nm excitation (Fig. 8): (A) When 4-MBA molecules directly contact Ag NPs, hot electrons excited by LSPR can be excited from Ag to the LUMO of 4-MBA. (B) Hot electrons from the Ag NPs may be injected to the semiconductors CB over the corresponding Schottky barrier and then transfer to the LUMO of 4-MBA molecules adsorbed on the metal oxides. (C) Electrons excited from the semiconductors VBs by the 532 nm laser beam to surface-states (E_{SS}), which commonly arise from defects such as oxygen vacancies and reduced metal ions at about 0.3–1.0 eV below the CB minimum for TiO_2[55] and WO_3[56] NPs, can be transferred to the LUMO of 4-MBA. The interfacial electron transfer between the co-assembled WO_3 and TiO_2 NPs can thereby provide an additional pathway to reduce charge recombination and enhance the substrate-to-molecule interaction, enabling ultrasensitive 4-MBA detection.

3.4 Benchmarking, selectivity, uniformity and reusability

According to the SERS intensity variation (Fig. 5 and 6), the lowest 4-MBA concentrations that could be detected were 10^{-12} and 10^{-13} M for the single Ag-PC287 TiO_2 and the composite Ag-PC287 4 : 1 substrate, respectively. In the latter case, the intensities of the dominant Raman peaks at 1079 and 1585 cm^{-1} and the 4-MBA concentrations showed very good linearity in log–log scales (adjusted R^2 coefficients of 0.9696 and 0.9815) over a wide concentration range of 10^{-4}–10^{-13} M (Fig. S8, ESI†). The lowest detected 4-MBA concentrations are lower than those reported for 4-MBA detection by plasmon-free as well as Ag-modified nanostructured metal oxide SERS substrates (Table 2), indicative of the ultrasensitive SERS efficiency of the hybrid Ag–WO_3/TiO_2 PC substrates. The average SERS enhancement factor (E_F) was estimated using the most intense 4-MBA vibration at 1585 cm^{-1} for the best performing Ag-PC287 4 : 1 substrates to reach 1.4×10^5, for 4-MBA concentration of 10^{-5} M (Fig. S5, ESI†).

In order to assess the universality/selectivity of the composite Ag–WO_3/TiO_2 PC films, the best performing Ag-PC287 4 : 1 film was tested in the SERS detection of R6G and MB cationic dyes (Fig. S9a, ESI†), which are commonly used analytes for evaluating new substrates as well as Raman reporter molecules for SERS sensors because of their high Raman cross-sections.[35] Highly sensitive detection of both R6G and MB dye molecules was obtained down to 10^{-11} and 10^{-9} M, respectively (Fig. 9).

These results validate the high SERS performance of Ag–WO_3/TiO_2 PC substrates under both resonant (R6G) and non-resonant (MB) excitation conditions, which can be further exploited in the fabrication of metal/metal oxide SERS-based immunosensors considering their limited selectivity to molecules containing thiol groups. The latter was explored by the direct SERS detection of GSH, which is the most abundant antioxidant in living organisms that contains non-protein thiol groups. As shown in Fig. S9b (ESI†), the GSH detection sensitivity of Ag-PC287 4 : 1 was limited to 1 mM, which stems from the very low Raman cross section of GSH that inhibits the label-free GSH detection by highly efficient SERS metal oxide[63] and plasmonic SERS substrates.[64] In this case, indirect detection of GSH can be pursued down to the nM level by replacing Raman labels, like R6G or 4-MBA, adsorbed onto the SERS substrate with GSH molecules, due to the stronger affinity between thiol groups and Ag NPs.[64]

To investigate the uniformity of the PC substrates, SERS spectra of 10^{-5} M 4-MBA were collected over 30 spots on the Ag-PC287 4 : 1 substrate, as shown in Fig. 10a and b. The Raman intensity of the 1585 cm^{-1} peak over the selected spots showed relatively small standard deviation equal to 13.8%. More importantly, the regeneration and reusability of the Ag–WO_3/TiO_2 PC substrates was also evaluated based on their inherent photocatalytic activity that can non-selectively degrade adsorbed analyte molecules.[13] Fig. 10c shows the SERS spectra obtained for 10^{-6} M of 4-MBA using the Ag-PC287 4 : 1 substrate over four successive UV-vis cleaning cycles. For each cycle, the SERS spectrum was first recorded on the PC substrate, which was then immersed in deionized water under UV-vis irradiation provided by a 300 W Xe lamp (100 mw cm^{-2}) for 30 min and then re-evaluated. The 4-MBA Raman bands disappeared completely after each UV-vis treatment, while the corresponding SERS signal could be recovered for every cycle verifying the

Table 2 SERS performance comparison for 4-MBA detection by TiO_2-based and Ag–TiO_2-based substrates (NPs: nanoparticles; NS: nanosheets; NFs: nanofibers; NR: nanorod; QDs: quantum dots)

Substrate	Morphology	Excitation wavelength (nm)	Lowest concentration (M)	Ref.
TiO_2	Mesoporous TiO_2 NPs	532	10^{-8}	48
TiO_2/rGO	TiO_2 NPs on reduced-GO NS	532	10^{-7}	57
TiO_2/ZnO	TiO_2 and ZnO NPs	633	10^{-8}	23
rGO/TiO_2/Fe_3O_4	Reduced-GO NS and TiO_2 NPs on Fe_3O_4	633	10^{-10}	58
Ni–TiO_2	Ni doped TiO_2 NPs	633	10^{-10}	59
Ag/TiO_2	TiO_2 NFs decorated with Ag NPs	532	10^{-7}	60
Ag–TiO_2	Hybrid Ag–TiO_2 NPs	633	10^{-9}	32
Ag/TiO_2	Core–shell NPs	785	1.2×10^{-10}	61
BP/Ag/TiO_2	Black phosphorus QDs and Ag NPs on TiO_2 NR arrays	532	10^{-12}	62
Ag–WO_3/TiO_2	Ag NPs on WO_3/TiO_2 inverse opals	532	10^{-13}	This work

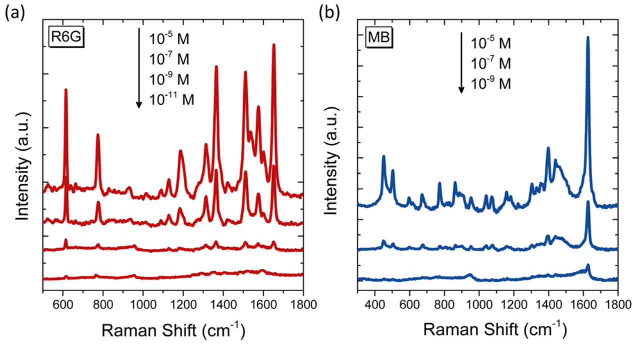

Fig. 9 SERS spectra of (a) R6G and (b) MB dye solutions of variable concentrations on the Ag-PC287 4 : 1 inverse opal substrates at 532 nm.

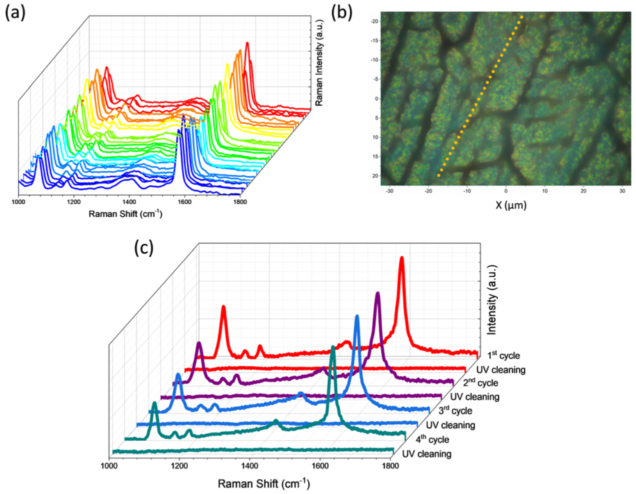

Fig. 10 (a) SERS spectra collected from 30 points for 10^{-5} M 4-MBA detection on the Ag-PC287 4 : 1 substrate along the yellow line shown in the (b) image of the selected area. (c) SERS spectra of 10^{-6} M 4-MBA on Ag-PC287 4 : 1 substrate for 4 cycles with intermediate UV-vis treatments.

excellent substrate recyclability that stems from the photocatalytic self-cleaning functionality of the Ag–WO_3/TiO_2 PC films.

4. Conclusions

In conclusion, single and heterostructured WO_3/TiO_2 inverse opal films can be efficiently utilized as PC supports of plasmonic Ag NPs for the fabrication of ultrasensitive, recyclable metal/semiconductor SERS substrates relying on the synergy of plasmonic amplification with slow photons and significantly improved CM enhancement *via* interfacial charge transfer. Composition and PBG tuning of the Ag-decorated WO_3/TiO_2 PCs resulted in ultrasensitive detection of 4-MBA as a non-resonant analyte down to 10^{-13} M for the optimal substrate with good uniformity and excellent recyclability stemming from its enhanced photocatalytic self-cleaning ability. Besides the dominant EM enhancement mechanism arising from the Ag LSPR, further assisted by spectral matching of the laser excitation with the PC slow photon regions, a major contribution to the SERS performance was concluded from the CM mechanism by means of cascade electron transfer from the plasmonic NPs to the metal oxide substrate and to the analyte molecules. This was most prominent for the best performing Ag–WO_3/TiO_2 PC substrates, which comprised a broad distribution of nanoscale type II heterojunctions in the metal oxide inverse opal walls and thus provided an additional charge transfer route to enhance the Ag–WO_3/TiO_2 - 4-MBA interaction. Semiconductor heterojunction formation along with PC structuring are accordingly proposed as a versatile approach to boost SERS performance by cooperative plasmonic/photonic/chemical enhancement mechanisms in hybrid metal/metal oxide SERS platforms.

Author contributions

Maria-Athina Apostolaki performed experimental investigations, formal analysis, methodology and writing of the original draft. Elias Sakellis and Spiros Gardelis contributed to the experimental investigations, formal analyses and results validation. Vlassis Likodimos contributed to the conceptualization, methodology, supervision, resources, writing – review & editing.

Data availability

The data supporting this article are included as part of the ESI.†

Conflicts of interest

There are no conflicts to declare.

Acknowledgements

The research work was supported by the Hellenic Foundation for Research and Innovation (HFRI) under the 3rd Call for HFRI PhD Fellowships (Fellowship Number: 5570).

References

1 T. Itoh, M. Procházka, Z. Dong, W. Ji, Y. S. Yamamoto, Y. Zhang and Y. Ozaki, *Chem. Rev.*, 2023, **123**, 1552.
2 J. Perumal, Y. Wang, A. B. E. Attia, U. S. Dinish and M. Olivo, *Nanoscale*, 2021, **13**, 553–580.
3 B. Li, S. Liu, L. Huang, M. Jin and J. Wang, *Coord. Chem. Rev.*, 2023, **494**, 215349.
4 T. T. X. Ong, E. W. Blanch and O. A. H. Jones, *Sci. Total Environ.*, 2020, **720**, 137601.
5 Y.-H. Huang, H. Wei, P. J. Santiago, W. J. Thrift, R. Ragan and S. Jiang, *Environ. Sci. Technol.*, 2023, **57**, 4880–4891.
6 C. Zong, M. Xu, L.-J. Xu, T. Wei, X. Ma, X.-S. Zheng, R. Hu and B. Ren, *Chem. Rev.*, 2018, **118**, 4946–4980.
7 K. B. Shanmugasundaram, J. Li, A. I. Sina, A. Wuethrich and M. Trau, *Mater. Adv.*, 2022, **3**, 1459–1471.
8 S.-Y. Ding, J. Yi, J.-F. Li, B. Ren, D.-Y. Wu, R. Panneerselvam and Z.-Q. Tian, *Nat. Rev. Mater.*, 2016, **1**, 1–16.

9 E. C. Le Ru and P. G. Etchegoin, *Principles of Surface Enhanced Raman Spectroscopy (and related Plasmonic Effects)*, Elsevier, Amsterdam, 2009.

10 N. Valley, N. Greeneltch, R. P. Van Duyne and G. C. Schatz, *J. Phys. Chem. Lett.*, 2013, **4**, 2599–2604.

11 X. Du, D. Liu, K. An, S. Jiang, Z. Wei, S. Wang, W. F. Ip and H. Pan, *Appl. Mater. Today*, 2022, **29**, 101563.

12 I. Alessandri and J. R. Lombardi, *Chem. Rev.*, 2016, **116**, 14921–14981.

13 Z. Zhang, S. Yang, R. Zhao, J. Chen, S. Wang, J. Choo and L. Chen, *ACS Sustainable Chem. Eng.*, 2023, **11**, 1278–1293.

14 J. R. Lombardi and R. L. Birke, *J. Phys. Chem. C*, 2014, **118**, 11120–11130.

15 X. X. Han, W. Ji, B. Zhao and Y. Ozaki, *Nanoscale*, 2017, **9**, 4847–4861.

16 L. Yang, X. Jiang, W. Ruan, B. Zhao, W. Xu and J. R. Lombardi, *J. Phys. Chem. C*, 2008, **112**, 20095–20098.

17 S. Cong, Y. Yuan, Z. Chen, J. Hou, M. Yang, Y. Su, Y. Zhang, L. Li, Q. Li, F. Geng and Z. Zhao, *Nat. Commun.*, 2015, **6**, 7800.

18 G. Song, W. Gong, S. Cong and Z. Zhao, *Angew. Chem., Int. Ed.*, 2021, **60**, 5505–5511.

19 J. Lin, Y. Shang, X. Li, J. Yu, X. Wang and L. Guo, *Adv. Mater.*, 2017, **29**, 1604797.

20 X. Wang, W. Shi, Z. Jin, W. Huang, J. Lin, G. Ma, S. Li and L. Guo, *Angew. Chem., Int. Ed.*, 2017, **129**, 9983–9987.

21 X. Wang, W. Shi, S. Wang, H. Zhao, J. Lin, Z. Yang, M. Chen and L. Guo, *J. Am. Chem. Soc.*, 2019, **141**, 5856–5862.

22 S. Xie, D. Chen, C. Gu, T. Jiang, S. Zeng, Y. Y. Wang, Z. Ni, X. Shen and J. Zhou, *ACS Appl. Mater. Interfaces*, 2021, **13**, 33345–33353.

23 X. Jiang, L. Xu, W. Ji, W. Wang, J. Du, L. Yang, W. Song, X. Han and B. Zhao, *Appl. Surf. Sci.*, 2022, **584**, 152609.

24 X. Tang, X. Fan, J. Zhou, S. Wang, M. Li, X. Hou, K. Jiang, Z. Ni, B. Zhao, Q. Hao and T. Qiu, *Nano Lett.*, 2023, **23**, 7037–7045.

25 X. Li, Y. Shang, J. Lin, A. Li, X. Wang, B. Li and L. Guo, *Adv. Funct. Mater.*, 2018, **28**, 1801868.

26 W. Ji, L. Li, W. Song, X. Wang, B. Zhao and Y. Ozaki, *Angew. Chem., Int. Ed.*, 2019, **58**, 14452–14456.

27 L. Yang, Y. Peng, Y. Yang, J. Liu, H. Huang, B. Yu, J. Zhao, Y. Lu, Z. Huang, Z. Li and J. R. Lombardi, *Adv. Sci.*, 2019, **6**, 1900310.

28 W. Ji, L. Li, J. Guan, M. Mu, W. Song, L. Sun, B. Zhao and Y. Ozaki, *Adv. Opt. Mater.*, 2021, **9**, 2101866.

29 J. Wang, P. W. H. Pinkse, L. I. Segerink and J. C. T. Eijkel, *ACS Nano*, 2021, **15**, 9299–9327.

30 D. Qi, L. Lu, L. Wang and J. Zhang, *J. Am. Chem. Soc.*, 2014, **136**, 9886–9889.

31 D. Papadakis, A. Diamantopoulou, P. A. Pantazopoulos, D. Palles, E. Sakellis, N. Boukos, N. Stefanou and V. Likodimos, *Nanoscale*, 2019, **11**, 21542–21553.

32 L. Yang, Q. Sang, J. Du, M. Yang, X. Li, Y. Shen, X. Han, X. Jiang and B. Zhao, *Phys. Chem. Chem. Phys.*, 2018, **20**, 15149–15157.

33 J. Wang, H. Le-The, T. Karamanos, R. N. S. Suryadharma, A. van den Berg, P. W. H. Pinkse, C. Rockstuhl, L. Shui, J. C. T. Eijkel and L. I. Segerink, *ACS Appl. Mater. Interfaces*, 2020, **12**, 37657–37669.

34 M.-A. Apostolaki, E. Sakellis, P. Tsipas, M. Giannouri, S. Gardelis, N. Boukos, A. Dimoulas and V. Likodimos, *Appl. Surf. Sci.*, 2023, **613**, 155919.

35 S. E. J. Bell, G. Charron, E. Cortés, J. Kneipp, M. L. de la Chapelle, J. Langer, M. Procházka, V. Tran and S. Schlücker, *Angew. Chem., Int. Ed.*, 2020, **59**, 5454–5462.

36 M. Sadakane, K. Sasaki, H. Kunioku, B. Ohtani, R. Abe and W. Ueda, *J. Mater. Chem.*, 2010, **20**, 1811–1818.

37 A. Toumazatou, M. Antoniadou, E. Sakellis, D. Tsoutsou, S. Gardelis, G. E. Romanos, N. Ioannidis, N. Boukos, A. Dimoulas, P. Falaras and V. Likodimos, *Mater. Adv.*, 2020, **1**, 2310–2322.

38 S. Balaji, Y. Djaoued and J. Robichaud, *J. Raman Spectrosc.*, 2006, **37**, 1416–1422.

39 M.-A. Apostolaki, A. Toumazatou, M. Antoniadou, E. Sakellis, E. Xenogiannopoulou, S. Gardelis, N. Boukos, P. Falaras, A. Dimoulas and V. Likodimos, *Nanomaterials*, 2020, **10**, 2566.

40 M. F. Daniel, B. Desbat, J. C. Lassegues, B. Gerand and M. Figlarz, *J. Solid State Chem.*, 1987, **67**, 235–247.

41 C. Santato, M. Odziemkowski, M. Ulmann and J. Augustynski, *J. Am. Chem. Soc.*, 2001, **123**, 10639–10649.

42 V. Likodimos, *Appl. Catal., B*, 2018, **230**, 269–303.

43 N. Stefanou and A. Modinos, *J. Phys.: Condens. Matter*, 1991, **3**, 8149–8157.

44 P. K. Jain and M. A. El-Sayed, *Chem. Phys. Lett.*, 2010, **487**, 153–164.

45 X. Jiang, X. L. Li, X. F. Jia, G. Z. Li, X. Wang, G. Y. Wang, Z. S. Li, L. B. Yang and B. Zhao, *J. Phys. Chem. C*, 2012, **116**, 14650–14655.

46 X. Xue, W. Ji, Z. Mao, H. Mao, Y. Wang, Xu Wang, W. Ruan, B. Zhao and J. R. Lombardi, *J. Phys. Chem. C*, 2012, **116**, 8792–8797.

47 X. Tang, X. Fan, L. Yao, G. Li, M. Li, X. Zhao, Q. Hao and T. Qiu, *J. Phys. Chem. Lett.*, 2022, **13**, 7816–7823.

48 L. Yang, D. Yin, Y. Shen, M. Yang, X. Li, X. Han, X. Jiang and B. Zhao, *Phys. Chem. Chem. Phys.*, 2017, **19**, 18731–18738.

49 O. L. Stroyuk, V. M. Dzhagan, A. V. Kozytskiy, A. Y. Breslavskiy, S. Y. Kuchmiy, A. Villabona and D. R. T. Zahn, *Mater. Sci. Semicond. Process.*, 2015, **37**, 3–8.

50 D. M. Maratos, A. Michail, A. Stamatelatos, S. Grammatikopoulos, D. Anestopoulos, V. Tangoulis, K. Papagelis, J. Parthenios and P. Poulopoulos, *Materials*, 2024, **17**, 4396.

51 M.-A. Apostolaki, E. Sakellis, P. Tsipas, S. Gardelis and V. Likodimos, *Proceedings*, 2024, vol. 97, p. 181.

52 Y. Yao, W. Guo, Z. Hui, C. Jin and P. Peng, *ChemistrySelect*, 2022, **7**, e202104357.

53 J. R. Lombardi and R. L. Birke, *J. Phys. Chem. C*, 2008, **112**, 5605–5617.

54 X. L. Zhang, Z. Yu, W. Ji, H. M. Sui, Q. Cong, X. Wang and B. Zhao, *J. Phys. Chem. C*, 2015, **119**, 22439–22444.

55 C. Di Valentin, G. Pacchioni and A. Selloni, *J. Phys. Chem. C*, 2009, **113**, 20543–20552.

56 M. Sachs, J. S. Park, E. Pastor, A. Kafizas, A. A. Wilson, L. Francàs, S. Gul, M. Ling, C. Blackman, J. Yano, A. Walsh and J. R. Durrant, *Chem. Sci.*, 2019, **10**, 5667–5677.

57 X. Jiang, D. Yina, M. Yang, J. Du, W. Wang, L. Zhang, L. Yang, X. Han and B. Zhao, *Appl. Surf. Sci.*, 2019, **487**, 938–944.

58 X. Jiang, Q. Sang, M. Yang, J. Du, W. Wang, L. Yang, X. Han and B. Zhao, *Phys. Chem. Chem. Phys.*, 2019, **21**, 12850.

59 X. Jiang, Y. Chen, J. Du, X. Li, Y. Shen, M. Yang, X. Han, L. Yang and B. Zhao, *J. Raman Spectrosc.*, 2018, **49**, 1257–1264.

60 Y. Zhao, L. Sun, M. Xi, Q. Feng, C. Jiang and H. Fong, *ACS Appl. Mater. Interfaces*, 2014, **6**, 5759–5767.

61 J. Yang, G. Song, L. Zhou, X. Wang, L. You and J. Li, *Appl. Surf. Sci.*, 2021, **539**, 147744.

62 J. Guo, C. Ding, W. Gan, P. Chen, M. Zhang and Z. Sun, *J. Alloys Compd.*, 2022, **918**, 165621.

63 I. Alessandri and L. E. Depero, *Small*, 2014, **10**, 1294–1298.

64 A. Kanioura, G. Geka, I. Kochylas, V. Likodimos, S. Gardelis, A. Dimitriou, N. Papanikolaou, S. Kakabakos and P. Petrou, *Biosensors*, 2023, **13**, 273.